

Spin-orbit effects in nanowire-based wurtzite semiconductor quantum dots

Guido A. Intronati,^{1,2,3} Pablo I. Tamborenea,¹ Dietmar Weinmann,² and Rodolfo A. Jalabert²

¹*Departamento de Física, Universidad de Buenos Aires, Ciudad Universitaria, Pab. I, C1428EHA Buenos Aires, Argentina*

²*IPCMS and NIE, UMR 7504, Université de Strasbourg – CNRS, 23 rue du Loess, BP 43, 67034 Strasbourg Cedex 2, France*

³*Service de Physique de l'État Condensé, CNRS URA 2464, CEA Saclay, 91191 Gif-sur-Yvette, France*

We study the effect of the Dresselhaus spin-orbit interaction on the electronic states and spin relaxation rates of cylindrical quantum dots defined on quantum wires having wurtzite lattice structure. The linear and cubic contributions of the bulk Dresselhaus spin-orbit coupling are taken into account, along with the influence of a weak external magnetic field. The previously found analytic solution for the electronic states of cylindrical quantum dots with zincblende lattice structures with Rashba interaction is extended to the case of quantum dots with wurtzite lattices. For the electronic states in InAs dots, we determine the spin texture and the effective g-factor, which shows a scaling collapse when plotted as a function of an effective renormalized dot-size dependent spin-orbit coupling strength. The acoustic-phonon-induced spin relaxation rate is calculated and the transverse piezoelectric potential is shown to be the dominant one.

PACS numbers: 73.21.La, 71.70.Ej, 73.61.Ey, 72.25.Rb,

I. INTRODUCTION

Semiconductor nanowires catalytically grown from nanoparticles, also called nanorods and nanowhiskers, provide a promising platform for spintronic devices. One of their advantages is that small quantum dots can be conveniently defined in these nanowires by employing different techniques. For example, quantum dots can be obtained by varying the composition during the growth process¹⁻³ in the same way that quasi-two-dimensional superlattices are grown using molecular-beam epitaxy or metalorganic chemical vapour deposition techniques. This fabrication method produces sharply defined quantum dots with square-well confinement in the longitudinal direction with highly controllable lengths. This type of quantum dot has been thoroughly studied in the last ten years and its spin-related properties have attracted much interest. In particular, the effective g-factor in InAs nanowire-based quantum dots has been measured⁴ for the first few electrons entering the dot and a strong dependence on the dot size has been established. Moreover, studies of spin-orbit interaction and spin relaxation have been made in InAs nanowire-based double-quantum dots with two electrons.^{5,6} A less precise but very flexible type of quantum-dot structure can be obtained by electrostatic confinement given by thin metallic gates deposited perpendicularly to the wires, typically made of InAs or InSb.⁷⁻⁹ The gate voltages, which are generally time-dependent, allow for the definition of the quantum dots as well as for the control of charge transport and spin manipulation via electric-dipole spin resonance (EDSR).^{7,10,11}

An important aspect of semiconductor nanorods, and also of the quantum dots defined in them, is that they often display the wurtzite crystal structure even though the constituting material has a zincblende structure in the bulk.¹² This structural change has important consequences for the spin properties of the dots. Notably, while in the zincblende semiconductors the leading Dresselhaus

spin-orbit coupling term is cubic in \mathbf{k} , in wurtzite crystals a linear term appears.¹³ A realistic theoretical study of the spin-orbit effects in wurtzite quantum dots has now become possible due to recent advances in the characterization of the band-structure of different wurtzite materials. While the linear-in- \mathbf{k} Dresselhaus contribution to the conduction band energy of wurtzite crystals has been known for some time,¹³ the cubic term in \mathbf{k} has been obtained only recently within the $\mathbf{k} \cdot \mathbf{p}$ approximation for different wurtzite semiconductors.^{14,15} De and Pryor,¹⁶ on the other hand, calculated the band-structure parameters of several binary compounds which normally display the zincblende structure in the bulk assuming that they have the wurtzite structure, in order to make them available for studies of wurtzite nanowires made of those same materials. These new data pave the way to a realistic study of nanowire-based quantum dots with wurtzite structure, which we undertake here.

Disk-shaped quantum dots with the Rashba structural spin-orbit interaction have been extensively studied theoretically and have been shown to admit an analytical solution for their energy eigenstates, without¹⁷ and with¹⁸ an applied perpendicular magnetic field. This solution, as we show here, can be conveniently extended to wurtzite quantum dots having cylindrical symmetry around the crystal c-axis, either with flat (“disk”) or elongated (“rod”) geometry. This is the case since the linear wurtzite Dresselhaus coupling is mathematically equivalent to the Rashba linear spin-orbit coupling characteristic of asymmetric semiconductor quantum wells, and furthermore, the newly obtained cubic term of wurtzite admits in the quasi-two-dimensional case the same eigenstates as the linear term. In this work we exploit these similarities in order to give solutions of the eigenvalue problem of the wurtzite quasi-two-dimensional structures and cylindrical quantum dots. In a confined geometry, the wurtzite cubic term of the Dresselhaus coupling gives rise to an additional linear contribution that reinforces or counteracts the bare linear term. As we will

see below, this reinforcement can be actually much bigger than the original linear term, opening up an unexplored regime of strong ‘‘Rashba-like’’ spin-orbit coupling in quantum wells and dots. Also, new possibilities appear when these linear Dresselhaus terms are combined with the standard Rashba term due to structural asymmetry. Indeed, further reinforcement or cancellations could possibly be achieved by tuning the symmetry and dimensions of the structure with the help of an external gate voltage. Thus, flexible schemes of spin-orbit coupling cancellation could be implemented leading to very long spin relaxation times in wurtzite structures having particular geometric shapes.¹⁹ The Dresselhaus term, enabled by the bulk inversion asymmetry, has been shown to yield the dominant coupling mechanism in cases of important structural asymmetry, like that of an extrinsic impurities giving rise to the impurity band of n-doped semiconductors.²⁰

The article is organized as follows. In Section II we introduce the effective Hamiltonian including the spin-orbit coupling for wurtzite structures. In Section III we obtain the electronic states of quasi-two-dimensional structures considering first only the linear spin-orbit coupling (Subsection III A) and then the full Hamiltonian with the cubic spin-orbit term and the Zeeman energy (Subsection III B). In Section IV the solution of the previous Section is used to solve the problem of thin cylindrical quantum dots with hard-wall confinement potential. In Subsection IV A we present the general analytical solution of this problem and the energy levels calculated numerically. In Subsection IV B we explore the spin structure of the one-particle eigenstates. The experimentally accessible effective g -factor of the quantum dots is studied in Subsection IV C, and in Subsection IV D we discuss the spin relaxation due to the coupling to phonons. Section V provides concluding remarks.

II. INTRINSIC SPIN-ORBIT COUPLING IN WURTZITE-BASED CONFINED GEOMETRIES

Within the envelope-function approximation for conduction-band electrons in wurtzite semiconductors, the effective quantum-dot Hamiltonian^{21,22} incorporating the linear¹³ and cubic^{14,15} Dresselhaus spin-orbit couplings reads

$$H = H_0 + H_1 + H_3 + H_Z, \quad (1)$$

$$H_0 = \frac{p^2}{2m^*} + V_c(x, y, z), \quad (2)$$

$$H_1 = \alpha (k_y \sigma_x - k_x \sigma_y), \quad (3)$$

$$H_3 = \gamma (bk_z^2 - k_x^2 - k_y^2) (k_y \sigma_x - k_x \sigma_y), \quad (4)$$

$$H_Z = \frac{1}{2} g^* \mu_B B \sigma_z, \quad (5)$$

where V_c is a nanoscale confinement potential, σ is the spin operator, α , γ , and b are material-dependent parameters, m^* is the effective mass and g^* the bulk effective gyromagnetic factor, μ_B is the Bohr magneton, and B is an external magnetic field assumed to be applied in the z -direction that coincides with the c -axis of the wurtzite structure. Here we include the magnetic field only through a Zeeman term since we will consider only relatively weak fields whose orbital effects can be safely ignored. In what follows we will consider quasi-two-dimensional and cylindrical quantum-dot structures. Catalytically grown nanorods made out of materials which have the zincblende crystal structure in the bulk can adopt either the zincblende or the wurtzite structure depending on the size of the nanoparticle seed and other growth conditions. Experimental data allowing to determine α , γ , and b are not yet available, so in our study we will rely on the theoretical estimates obtained by De and Pryor.¹⁶ Motivated by anticipated applications to nanowires, these authors calculated all the relevant band-structure parameters assuming a wurtzite structure for the semiconductor binary compounds that have a zincblende structure in the bulk. An asymmetry in the z -confinement would add a Rashba term, resulting in a renormalization of α . In order to give a wider applicability to our results, whenever possible we will present them for reasonably large ranges of parameters so that they can be adapted to different materials and to parameters newly obtained, experimentally or theoretically.

III. QUASI-TWO-DIMENSIONAL SYSTEMS

Before tackling the quantum-dot problem it is useful to consider the eigenvalue problem of a quasi-two-dimensional system. Thus, we choose $V_c = V_c(z)$ which confines the electrons only along the z -direction, such that H_0 can be separated as $H_0 = H_0^{xy} + H_0^z$, with an in-plane term $H_0^{xy} = (p_x^2 + p_y^2)/2m^*$ and a longitudinal part defined by $H_0^z = p_z^2/2m^* + V_c(z)$.

A. Linear term

If we leave aside for the moment the cubic term H_3 and the external magnetic field, we are left with a situation mathematically analogous to the classic Rashba problem in which the spin-orbit coupling originates from an asymmetric extrinsic potential. Since the total Hamiltonian is separable we can start working with the two-dimensional problem in the (x, y) plane given by $H_{2d} = H_0^{xy} + H_1$. Its well-known solution is²³

$$\zeta_{\mathbf{k}s}(\mathbf{r}) = \frac{1}{\sqrt{2A}} e^{i\mathbf{k}\cdot\mathbf{r}} \begin{pmatrix} s e^{-i(\varphi_{\mathbf{k}} - \frac{\pi}{2})} \\ 1 \end{pmatrix}, \quad (6)$$

$$E(k, s) = \frac{\hbar^2 k^2}{2m^*} - s\alpha k. \quad (7)$$

In these expressions and henceforth, A is the area of the sample, $\mathbf{r} = (x, y)$, $\mathbf{k} = (k_x, k_y)$, $k = \sqrt{k_x^2 + k_y^2}$, and φ_k is the angle of \mathbf{k} in polar coordinates. The spin quantum number $s = \pm 1$ denotes spin-up and spin-down eigenstates with respect to the spin quantization axis which lies in the xy -plane and is perpendicular to \mathbf{k} with a polar angle $\varphi_k - \pi/2$. Note that the spin-orbit term in the energy has a minus sign compared to the usual Rashba expression, coming from the minus sign used in Eq. (3). The states (6) are degenerate for given k and s . This plane-wave solution is convenient in most contexts and has the advantage that its spin quantization direction is position independent. However, (6) does not profit from the fact that the z -component of the total angular momentum J_z commutes with the Hamiltonian and therefore provides a good quantum number, which is an extremely useful property when one tackles cylindrically symmetric nanostructures. The common eigenstates of H_{2d} and J_z are given by¹⁷

$$\chi_{m,k,s}(r, \varphi) = \begin{pmatrix} J_m(kr) e^{im\varphi} \\ s J_{m+1}(kr) e^{i(m+1)\varphi} \end{pmatrix}. \quad (8)$$

The states (8) are degenerate with those of (6) for given k and s , and can be expressed as superpositions of them. Note that while the spin of the basis states (6) lies always in the xy -plane, that is not the case for the states (8), which are superpositions of the states (6) within degenerate subspaces. Furthermore, the spin direction in the latter is space-dependent while in the former it is not.

where

$$\nabla_m^2 \equiv \frac{1}{\rho} \frac{\partial}{\partial \rho} + \frac{\partial^2}{\partial \rho^2} - \frac{m^2}{\rho^2}. \quad (14)$$

In Eqs. (13) we have introduced R , a parameter to be defined in the quantum dot context, and $u_E = \hbar^2/2m^*R^2$, as units of length and energy, respectively. This allows us to define the dimensionless parameters $\rho = r/R$, $K = kR$, $\gamma' = \gamma/u_E R^3$, and $h = g\mu_B B/2u_E$. The dependence on the (“longitudinal”) quantum number n has been incorporated to the in-plane problem via the redef-

B. Cubic term

Let us now include the cubic-in- k term of the Hamiltonian, H_3 , given in Eq. (4), and the Zeeman energy, Eq. (5). As usual, we work in the envelope-function approximation where the Hamiltonian H is expressed by replacing \mathbf{k} by $-i\nabla$. We adopt cylindrical coordinates (r, φ, z) and for the in-plane coordinates we have

$$H = -\frac{\hbar^2}{2m^*} \left(\nabla^2 + \frac{\partial^2}{\partial z^2} \right) + V_c(z) + H_1 + \frac{\gamma}{\alpha} \left[b \left(-\frac{\partial^2}{\partial z^2} \right) + \nabla^2 \right] H_1 + H_Z. \quad (9)$$

where the symbol ∇^2 is used to represent the two-dimensional Laplacian.

Assuming that $V_c(z)$ is an infinite potential well of length L , the proposed solution of the Schrödinger equation $H\xi = E\xi$ is

$$\xi_{nm}(r, \varphi, z) = \psi_{nm}(r, \varphi) \sqrt{\frac{2}{L}} \sin\left(\frac{n\pi z}{L}\right), \quad (10)$$

$$\psi_{nm}(r, \varphi) = \begin{pmatrix} u_{nm}(r) e^{im\varphi} \\ v_{nm}(r) e^{i(m+1)\varphi} \end{pmatrix}, \quad (11)$$

where $u_{nm}(r)$ and $v_{nm}(r)$ are real functions and $\psi_{nm}(r, \varphi)$ is an eigenstate of J_z with eigenvalue $j_z = m + 1/2$. The corresponding total energy is

$$E_n^t = E_n + E_n^z, \quad (12)$$

with the radial part E_n and the longitudinal energy $E_n^z = (\hbar^2/2m^*)(n\pi/L)^2$ that is due to the confinement in the z -direction. Plugging (10) into the Schrödinger equation we obtain for u_{nm} and v_{nm} the equations

$$(-\nabla_m^2 + h) u_{nm}(\rho) + (\alpha'_n + \gamma' \nabla_m^2) \left(\frac{m+1}{\rho} + \frac{\partial}{\partial \rho} \right) v_{nm}(\rho) = \varepsilon_n u_{nm}(\rho) \quad (13a)$$

$$(-\nabla_{m+1}^2 - h) v_{nm}(\rho) + (\alpha'_n + \gamma' \nabla_{m+1}^2) \left(\frac{m}{\rho} - \frac{\partial}{\partial \rho} \right) u_{nm}(\rho) = \varepsilon_n v_{nm}(\rho) \quad (13b)$$

inition of the coupling constant α written in the dimensionless form

$$\alpha'_n = \left[\alpha + \gamma b \left(\frac{n\pi}{L} \right)^2 \right] / u_E R, \quad (15)$$

and the in-plane dimensionless energy is given by $\varepsilon_n = E_n/u_E$.

To solve Eqs. (13) we make the ansatz

$$u_{nm}(\rho) = J_m(K\rho), \quad v_{nm}(\rho) = d_n J_{m+1}(K\rho). \quad (16)$$

Using the well-known properties of the Bessel functions²⁴

$$\left(\frac{m}{\rho} - \frac{\partial}{\partial \rho}\right) J_m(K\rho) = K J_{m+1}(K\rho), \quad (17a)$$

$$\left(\frac{m+1}{\rho} + \frac{\partial}{\partial \rho}\right) J_{m+1}(K\rho) = K J_m(K\rho), \quad (17b)$$

one obtains from (13) the eigenvalue equation

$$\begin{pmatrix} K^2 + h - \varepsilon_n & \alpha'_n K - \gamma' K^3 \\ \alpha'_n K - \gamma' K^3 & K^2 - h - \varepsilon_n \end{pmatrix} \begin{pmatrix} 1 \\ d_n \end{pmatrix} = 0, \quad (18)$$

whose solutions are

$$\varepsilon_{n\pm} = K^2 \pm \sqrt{K^2 (\alpha'_n - \gamma' K^2)^2 + h^2}. \quad (19)$$

Then, the total energy is given by

$$E_{n\pm}^t = (\varepsilon_{n\pm} + \varepsilon_n^z) u_E, \quad (20)$$

with $\varepsilon_n^z = E_n^z / u_E = (n\pi R/L)^2$, and the corresponding wave functions are

$$\psi_{Knm}(\rho, \varphi) = \begin{pmatrix} J_m(K\rho) e^{im\varphi} \\ d_{n\pm} J_{m+1}(K\rho) e^{i(m+1)\varphi} \end{pmatrix}, \quad (21)$$

with

$$d_{n\pm} = \frac{\varepsilon_{n\pm} - K^2 - h}{\alpha'_n K - \gamma' K^3}. \quad (22)$$

The obtained solution, Eqs. (19) and (21), reduces to the one of the linear Hamiltonian analyzed in Sec. III A, given by Eqs. (7) and (8), when the cubic term and the Zeeman energy are neglected. As in the linear Rashba-like problem, there are two possible energies $\varepsilon_{n\pm}$ for a given value of K . The energies $\varepsilon_{n\pm}$ can be expressed as a function of K^2 and are thus independent of the sign of K . Because of the (anti-)symmetry of the Bessel functions with respect to a change of sign in the argument, the wave functions corresponding to $\pm K$ are not independent. We therefore keep only positive values of K .

In the presence of a magnetic field, and for in-plane energies ε_n close to zero, Eq. (19) has solutions with imaginary $K = i\kappa$. Since $J_m(i\kappa\rho) = i^m I_m(\kappa\rho)$, where I_m is the modified Bessel function of the first kind of order m , the corresponding wave functions grow exponentially with increasing ρ and are thus not normalizable in an infinitely large system. Such solutions are therefore discarded in the context of two-dimensional systems, but they will become relevant for the case of quantum dots discussed in Sec. IV.

In Fig. 1 we present (solid lines) the dispersion relation (20) for InAs with the parameters suggested in Ref. [16] from band-structure calculations (we label them with an index r)

$$\alpha_r = 0.571 \text{ eV}\text{\AA} \quad \gamma_r = 571.8 \text{ eV}\text{\AA}^3,$$

$b = 4$ and an effective mass $m^* = 0.026 m_e$.⁴ The two energy branches are plotted for $B = 0$ T (left) and $B = 20$ T

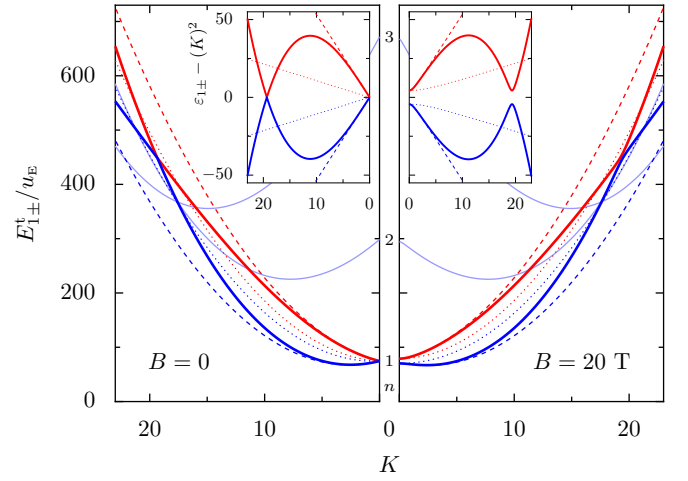


FIG. 1. Energy dispersion [Eq. (20)] with (right) and without magnetic field (left). For subband $n = 1$, three cases are considered: thick solid lines correspond to the full SOC, dashed lines to an intermediate case with no cubic-in- \mathbf{k} SOC, but with the α parameter renormalized by γ (15), and dotted lines to the bare Rashba-like interaction, linear in \mathbf{k} . Blue (red) lines correspond to ε_{n-} (ε_{n+}). The thinner solid lines are the lower branches of subbands $n = 2$ and 3 . *Inset*: Same three cases of SOC dispersion relation without the parabolic contribution for $n = 1$. The Zeeman effect and an avoided crossing are more clearly distinguished on this energy scale.

(right). (In this figure we consider a large value of the magnetic field with the sole purpose of illustrating more clearly its effects on the energy levels.) We also show the effect of suppressing the cubic term, but keeping the contribution of γ in Eq. (15) on the linear term (dashed line), as well as the usual Rashba-like case obtained for $\gamma = 0$ (dotted line). Blue (red) lines correspond to ε_{n-} (ε_{n+}). Thick lines correspond to $n = 1$, as indicated between the two panels. Also shown are the curves of ε_{2-} and ε_{3-} including the linear and cubic spin-orbit contributions (thin lines). For $n = 1$ and $B = 0$ T there is a crossing of the two branches at $K = \sqrt{\alpha'/\gamma'}$ ($K = 19.34$ in our plot). An analogous feature present in bulk wurtzite semiconductors has been discussed in the literature as a possible opportunity to implement long-lived spin qubits.²⁵ The crossing becomes avoided for finite B , although the level splitting can hardly be seen on the right panel of Fig. 1. For this reason we plot in the inset the energies subtracting the trivial parabolic contribution. This allows for a smaller energy range such that one can clearly observe the Zeeman splitting at $K = 0$ and the avoided crossing.

In Fig. 1, the thin solid lines are the lower branches of subbands $n = 2$ and 3 . Even though they lie at sufficiently high energies so as not to affect our further analysis, which concentrates on low energies, we note that they could become relevant if the region of the avoided crossing mentioned above is explored. Also, we point out a potentially interesting degeneracy point of all the lower branches of the different subbands, which happens at $K = 1/b\gamma'$ ($K = 17.58$ in our plot), where the curves

become independent of n . This massive degeneracy is due to the renormalized linear spin-orbit term. Although this feature may be physically relevant, we mention that higher values of n correspond to higher k_z and eventually the energies of Eq. (20) obtained in third-order perturbation theory in wave-vector cease to be reliable.

IV. QUANTUM DOTS

A. Effect of spin-orbit coupling on the energy levels

We now consider cylindrical quantum-dots with hard-wall quantum confinement having radius R and length L . The discrete eigenenergies and states of this problem will be obtained from the quantum-well solutions found in the previous Section. In order to get the energetically lowest states, we keep only the lowest subband, $n = 1$, and omit the subindex n from now on. In all cases we work with k low enough to stay in the regime of validity of the expansion of the effective SOC Hamiltonian up to

3rd order in k .

The eigenstates of the disk-shaped quantum dot have to satisfy the circular boundary condition (the hard-wall confinement forces a zero of the wave function at the dot boundary). This can be achieved at particular values of the in-plane energy ε for linear combinations $\Psi_m = c_a \psi_{K_a m} + c_b \psi_{K_b m}$ of two degenerate eigenstates of the quantum-well problem. Those quantized energies are then the eigenenergies of the quantum dot. In the general case including a finite magnetic field, there are three energy ranges (see Fig. 1) with different situations: i) energies in the low ‘‘belly’’ of the ε_- branch, $\varepsilon < -|h|$; ii) energies above the energy gap caused at $K = 0$ by the Zeeman splitting, $\varepsilon > |h|$; iii) energies in the Zeeman gap, $-|h| < \varepsilon < |h|$. We now consider these three cases separately.

Case i) $\varepsilon < -|h|$: two real values of K , noted K_a and K_b , associated to the ε_- branch (in the ‘‘belly’’ region) are involved in the dot solution. The in-plane wave function is thus written as

$$\Psi_m(\rho, \varphi) = c_a \begin{pmatrix} J_m(K_a \rho) e^{im\varphi} \\ d_-(K_a) J_{m+1}(K_a \rho) e^{i(m+1)\varphi} \end{pmatrix} + c_b \begin{pmatrix} J_m(K_b \rho) e^{im\varphi} \\ d_-(K_b) J_{m+1}(K_b \rho) e^{i(m+1)\varphi} \end{pmatrix}, \quad (23)$$

with the hard-wall boundary condition $\Psi_m(\rho = 1, \varphi) = 0$. A non-trivial solution (K_a, K_b) will be given by the condition

$$J_m(K_a) d_-(K_b) J_{m+1}(K_b) - J_m(K_b) d_-(K_a) J_{m+1}(K_a) = 0. \quad (24)$$

Case ii) $\varepsilon > |h|$: the two quantum-well states involved in the dot solution belong to different branches, ε_+ and ε_- , with real values of K , noted K_a and K_b :

$$\Psi_m(\rho, \varphi) = c_a \begin{pmatrix} J_m(K_a \rho) e^{im\varphi} \\ d_+(K_a) J_{m+1}(K_a \rho) e^{i(m+1)\varphi} \end{pmatrix} + c_b \begin{pmatrix} J_m(K_b \rho) e^{im\varphi} \\ d_-(K_b) J_{m+1}(K_b \rho) e^{i(m+1)\varphi} \end{pmatrix}, \quad (25)$$

The boundary condition leads to

$$J_m(K_a) d_-(K_b) J_{m+1}(K_b) - J_m(K_b) d_+(K_a) J_{m+1}(K_a) = 0. \quad (26)$$

Case iii) $-|h| < \varepsilon < |h|$: one imaginary value of K , $K_a \equiv i\kappa_a$, and a real value K_b are involved. The energy associated to K_a is

$$\varepsilon_{\pm, a} = -\kappa_a^2 \pm \sqrt{-\kappa_a^2 (\alpha'_n + \gamma' \kappa_a^2)^2 + h^2}, \quad (27)$$

and the coefficient for the wave function

$$d_{\pm}(K_a) = (-i) \frac{\varepsilon_{\pm, a} + \kappa_a^2 - h}{\alpha'_n \kappa_a + \gamma' \kappa_a^3} \equiv -i \delta_{\pm}(\kappa_a). \quad (28)$$

With $J_m(i\kappa\rho) = i^m I_m(\kappa\rho)$, the quantum-dot wave function is then written as

$$\Psi_m(\rho, \varphi) = i^m c_a \begin{pmatrix} I_m(\kappa_a \rho) e^{im\varphi} \\ \delta_{\pm}(\kappa_a) I_{m+1}(\kappa_a \rho) e^{i(m+1)\varphi} \end{pmatrix} + c_b \begin{pmatrix} J_m(K_b \rho) e^{im\varphi} \\ d_-(K_b) J_{m+1}(K_b \rho) e^{i(m+1)\varphi} \end{pmatrix}. \quad (29)$$

The boundary condition leads to

$$I_m(\kappa_a) d_-(K_b) J_{m+1}(K_b) - J_m(K_b) \delta_{\pm}(\kappa_a) I_{m+1}(\kappa_a) = 0. \quad (30)$$

Equations (24), (26), and (30) express a root-finding problem, which we solve numerically. We find a family

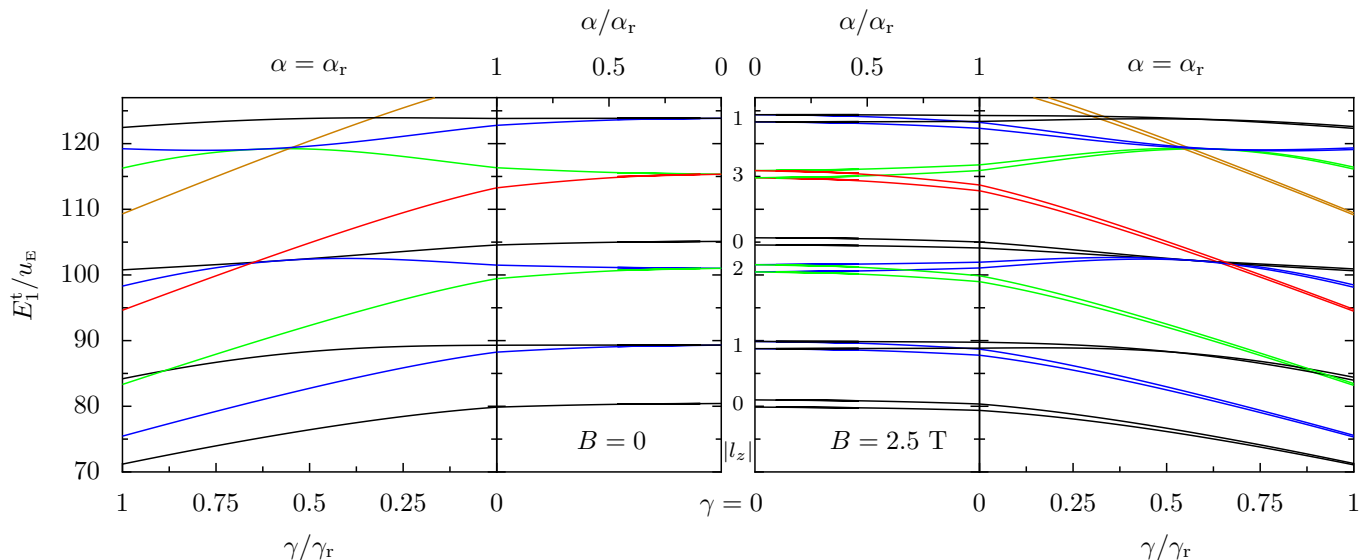


FIG. 2. The discrete eigenenergies of a quantum dot with radius $R = 275 \text{ \AA}$ and height $L = 100 \text{ \AA}$ for $n = 1$, shown as a function of the spin-orbit coupling strengths α and γ , without magnetic field (left side) and with $B = 2.5 \text{ T}$ (right side). States with $|j_z| = 1/2, 3/2, 5/2, 7/5$, and $9/5$ are represented by different black, blue, green, red, and orange lines, respectively. In the central panels we keep $\gamma = 0$ and vary α from zero up to $\alpha_r = 0.571 \text{ eV\AA}$, reported in [16]. Conversely, in the following curves (outside panels) α is fixed at α_r , and γ increases from zero to its final value of $\gamma_r = 571.8 \text{ eV\AA}^3$. In-between the panels, the values of the quantum numbers l_z associated to the nearby states at zero SOC are indicated.

of solutions for each value of m that correspond to the discretized energies of the quantum dot. Moreover, the solutions give access to the wave numbers $\{K_a, K_b\}$ such that we can determine the coefficients $\{c_a, c_b\}$ from the boundary condition and the normalization of the in-plane wave functions (23), (25), and (29). All of these solutions carry a well-defined value of $j_z = m + 1/2$, and in the absence of a magnetic field, the j_z and $-j_z$ solutions are degenerate.

The results for the energy levels are presented in Fig. 2 as a function of the SOC coupling strength. The states of different $|j_z|$ are shown with different colors. To show the effect of the spin-orbit coupling, we start from the case of vanishing SOC in the center of the figure and increase the SOC strength up to the predicted values α_r and γ_r corresponding to the left and right edge of the figure.

Without SOC ($\alpha = \gamma = 0$, inner edges of the plot), the electronic states can be characterized by the orbital angular momentum l_z along the z -axis and the spin $s = \pm 1/2$, in addition to the total angular momentum $j_z = l_z + s$. The values of $|l_z|$ corresponding to the states are indicated in the center of the figure. Without magnetic field (left side), the states characterized by $(l_z, s) = (\pm |l_z|, \pm 1/2)$ are degenerate. In the presence of a magnetic field (right side), the Zeeman energy splits the levels corresponding different spin orientations. In the presence of SOC, the orbital angular momentum and the spin get mixed, l_z and s cease to be good quantum numbers, and only the total angular momentum quantum number j_z , shown by the different colors in Fig. 2 characterizes the states. It can be seen states corresponding to

the same $|l_z|$ at zero SOC are split by the SOC according to the different values of $|j_z|$.

In order to discriminate the effects of the different SOC terms, we increase the SOC in two steps. We first consider the usual Rashba-like problem by setting $\gamma = 0$ and varying the linear coupling strength α from zero up to $\alpha_r = 0.571 \text{ eV\AA}$. This situation is depicted in the inner part of Fig. 2, where the left side corresponds to the case of zero magnetic field and the right side to $B = 2.5 \text{ T}$. The ensuing step is to fix α at α_r and raise the value of γ from zero to $\gamma_r = 571.8 \text{ eV\AA}^3$. The result is matched with the previous one and traced by the adjoining curves in the outer panels of the figure. It must be noted that γ determines not only the cubic-in- k SOC coupling, but it also enters in the linear-in- k coupling [cf. Eq. (15)]. Consequently, at the end of each curve we find the energy of the quantum dot for the corresponding α_r and γ_r .

Note the significant effect of γ on the eigenenergies, that leads to much stronger energy changes than α alone. It brings, for example, the lowest pair of levels with $j_z = \pm 1/2$ (lowest black curves) down to energies that are below E_1^z . Moreover, level crossings occur as a function of γ , changing the order of the states in energy with respect to the case of vanishing SOC. This happens mainly for the lowest energy states of a given $|j_z|$ that are pulled down by the SOC below the higher energy states with lower values of $|j_z|$. We remark that the full range of eigenenergies that we consider has not been explored in previous studies, and that we explicitly include allowed energy values that lie within the gap of the two-dimensional dispersion relation of Fig. 1, that

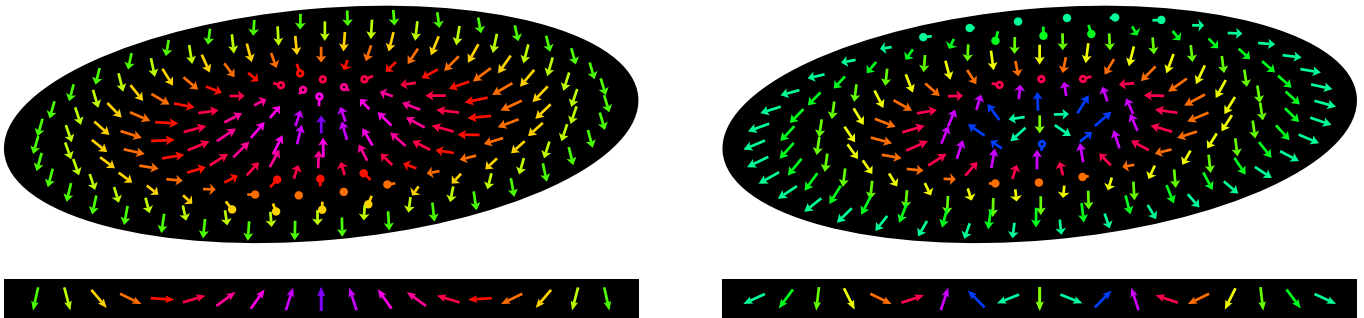


FIG. 3. Spin textures in cylindrical quantum dots with $L = 100 \text{ \AA}$ and $R = 275 \text{ \AA}$. Left and right panels show results for the lowest and the second lowest states with $|j_z| = 1/2$. The arrows and colors indicate the spin orientation as a function of the position in the xy -plane. Below the disks, the same data are shown for a linear cut through the center of the sample.

is $-|h| < \varepsilon_1 < |h|$. It can also be observed that the Zeeman splitting shrinks as the SOC increases, while the spin mixture brought about by the latter increases accordingly. This indicates that the effective g-factor in quantum dots is affected by the SOC and depends on the geometry.

B. Spin texture of the eigenstates

We now investigate the properties of the quantum dot eigenstates. The spinor states of Eqs. (23), (25), and (29) contain the information on the spin texture of the dot states. Without SOC and in the presence of a magnetic field, even a very weak one, the states are spin polarized, and the spin texture of the one-electron states is uniform throughout the dot. The appearance of a non-trivial spin texture is therefore a signature of the SOC, and can be seen as the degree of mixing of the two spin components in an eigenspinor. To obtain the spin texture corresponding to a state, we compute the expectation value of the spin operator

$$\langle \boldsymbol{\sigma} \rangle(\mathbf{r}) = \Psi^\dagger(\mathbf{r}) \boldsymbol{\sigma} \Psi(\mathbf{r}) \quad (31)$$

for each spatial point \mathbf{r} inside the quantum dot. Because of the separability of the wave functions (10), the spin orientation is independent of the longitudinal coordinate z . Moreover, the rotational symmetry of the dots around the z -axis imposes that the resulting spin orientations present the same symmetry. Therefore, their projection on the $\hat{\varphi}$ -direction vanishes, such that the local spin direction

$$\langle \boldsymbol{\sigma} \rangle(\mathbf{r}) = \hat{r} \cos[\beta(r)] + \hat{z} \sin[\beta(r)] \quad (32)$$

has only radial and z -components. The angle of the local spin orientation with respect to the xy -plane β depends only on the radial coordinate r . We construct the full eigenstate solution Ψ with energy ε as (23), (25), and (29), depending on the value of ε , with the corresponding $K_a(\varepsilon)$ and $K_b(\varepsilon)$ obtained from a numerical solution of the quantization conditions (24), (26), or (30).

In Fig. 3, we present two examples of spin texture in cylindrical quantum dots of length $L = 100 \text{ \AA}$ and radius $R = 275 \text{ \AA}$, in the presence of the full linear and the cubic SOC terms with the coupling strengths α_r and γ_r predicted in Ref. [16]. The left panels show the dependence of the spin orientation on the position in the xy -plane for the lowest energy states that have $|j_z| = 1/2$. This spin texture corresponds to one of the two sublevels in the lowest Zeeman doublet, shown in Fig. 2 by the two lowest black lines. The other of the sublevels, that are degenerate at $B = 0$, has spin orientations with the sign of the z -component reversed. The right panels show the spin texture for the next higher levels that are characterized by $|j_z| = 1/2$, corresponding to the second pair of levels (black lines starting at $|l_z| = 1$ in Fig. 2).

C. Effective g-factor in quantum dots

The effective g-factor is experimentally accessible, and it is thus a widely studied quantity. An example are the measurements of Ref. [4], where the effective g-factor has been observed to depend on the dot size with absolute values that are reduced as compared to the bulk effective g-factor $g^* \approx -14.7$ (value from Ref. [26]). In the experiment, the effective g-factor is extracted from the linear term of the magnetic-field induced energy splitting

$$\Delta E = |g_{\text{eff}} \mu_B B| \quad (33)$$

of two states that are characterized by the same $|j_z|$ and degenerate in the absence of a magnetic field. According to this definition, each quantum-dot state has its own effective g-factor, and we will focus on the effective g-factor of the ground state which is often the most relevant one. To calculate the effective g-factor we can use different approaches. The most direct way is to set the magnetic field strength to a small finite value, e.g. $B = 0.1 \text{ T}$, and to calculate the difference between the two lowest dot energies, using the procedure of Sec. IV A. Alternatively, in order to avoid the finite value of the magnetic field, we

can express the effective g-factor as

$$g_{\text{eff}} = \frac{1}{\mu_B} \frac{\partial \Delta E}{\partial B} = g^* \frac{\partial \varepsilon}{\partial h} \quad (34)$$

in terms of the sensitivity $\partial \varepsilon / \partial h$ of the quantized dot energy levels with respect to the magnetic field, at $h =$

$$g_{\text{eff}} = -g^* \frac{\text{sgn}(\varepsilon)u(K_a) + u(K_b)}{u(K_a)u(K_b)} \times \frac{J_m(K_a)J_{m+1}(K_b)}{\zeta(K_a, K_b) [2K_a + \text{sgn}(\varepsilon)u'(K_a)]^{-1} + \text{sgn}(\varepsilon)\zeta(K_b, K_a) [2K_b - u'(K_b)]^{-1}}, \quad (35)$$

where we have defined the functions

$$\zeta(K_a, K_b) = J_m(K_b)J'_{m+1}(K_a) + \text{sgn}(\varepsilon)J'_m(K_a)J_{m+1}(K_b) \quad (36)$$

and $u(K) = \alpha'K - \gamma'K^3$. We denote by $J'_m(K)$ and $u'(K)$ the derivatives of the functions J_m and u with respect to K .

The expression of Eq. (35) is a generalization of the result of Ref. [18], and it reduces to the result given in Eq. (13) of that paper in the case $\gamma = 0$ of vanishing cubic-in- \mathbf{k} SOC. In order to compute the effective g-factor using the analytic expression (35), we first determine the eigenenergies and the corresponding pair of wave-vectors K_a and K_b by solving numerically the quantization condition of Eqs. (24) and (26) at $h = 0$, and then evaluate (35) using the obtained values. In Fig. 4 we present our results for different dot dimensions with lengths ranging from 50 Å to 200 Å and radii from 150 Å to 500 Å. We have checked that a direct numerical evaluation of the level splitting from numerically calculated energies at small values of magnetic field B yields the same results as Eq. (35). In the figure, the numerical data for g_{eff} (black dots) is plotted as a function of the inverse effective dimensionless linear in-plane spin-orbit coupling α'^{-1} (see Eq. (15)). The data corresponding to different dot sizes approximately collapses on a single curve. While a plot as a function of α' shows the same data collapse, the presentation of Fig. 4 allows for greater clarity in the comparison with experiment. Such a single-parameter scaling shows that the dependence of the ground state effective g-factor g_{eff} on L and R is, at least within the range of explored sizes, to a good approximation given by a function of α' . Thus, the main mechanism giving rise to a size-dependence of the effective ground-state g-factor is the L -dependent renormalization of the effective linear coupling strength α' by the cubic SOC γ , and its scaling with R .

For a fixed value of L , the renormalized linear-in- k coupling strength α' is proportional to $1/u_E R$. Since $u_E \propto R^{-2}$, we have $\alpha' \propto R$ such that the effective linear coupling decreases with decreasing R . It can be seen in Fig. 4 that the value of g_{eff} increases (in absolute value)

0. To determine this derivative, we proceed as in the case of Rashba SOC treated in Ref. [18], and derive the quantization conditions (24) and (26) for negative and positive in-plane energy ε , respectively. The resulting expression for the effective g-factor is

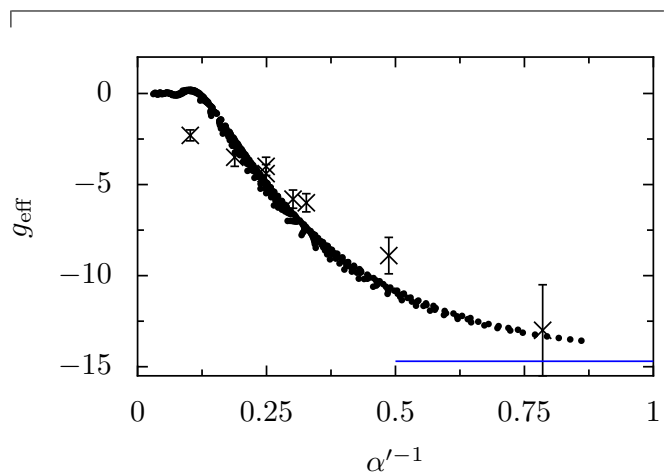


FIG. 4. The calculated effective g-factors (full black circles) for cylindrical quantum dots of different length L and radius R , plotted versus $1/\alpha'$ defined in (15), with the SOC parameters from Ref. [16]. The data points are for dots with radii R from 150 Å to 500 Å, and lengths values L in the range between 50 Å and 200 Å. The crosses represent experimental data from Ref. [4], obtained with a magnetic field perpendicular to the symmetry axis of the quantum dot. The blue horizontal line indicates the bulk effective value $g^* \approx -14.7$.

towards the bulk effective g-factor g^* (blue line) as R and thus the effective coupling α' decreases. An increase in R leads to a larger α' , and according to Fig. 2, the Zeeman splitting of the levels decreases as the SOC increases. The consequence is that $|g_{\text{eff}}|$ diminishes. Conversely, for a given radius R , the increase in L leads to a decrease of the effective linear-in- k coupling α' , with the result of an approach of g_{eff} to g^* .

The effective cubic-in- k coupling $\gamma' \propto 1/u_E R^3 \propto 1/R$ increases when R decreases, and a competition between α' and γ' can be expected. However, the spectrum of the lowest energies is related to small values of K and mainly dominated by the linear SOC (see Fig. 1), at least for the

not too small values of R that we consider. The scaling of the results with α' leads to the conclusion that the main effect of the cubic Dresselhaus coupling γ is the renormalization of the effective linear-in- k coupling, and that the impact of the effective cubic-in- k coupling strength γ' seems to be of minor importance. However, the above arguments are relevant for the case under study of not too small R and low-energy dot states. More important effects of the cubic-in- k coupling γ' can be expected for the g-factor of excited states and in dots with very small R .

Similarly to the results presented in Ref. [26], where a zincblende Hamiltonian with adjustable parameters such as the energy band gap magnitude was used, we find negative values for the ground state g-factor of the dot. However, in our case small positive values do occur for short pillbox-shaped dots. In general, and similarly to the theoretical results for Rashba SOC¹⁸ as well as the experimental values of Ref. [4] (crosses in Fig. 4), our effective g-factors are of reduced absolute value as compared to the bulk effective g-factor g^* . While the qualitative behavior and size-dependence of our results are clearly consistent with the data of Ref. [4], a direct quantitative comparison cannot be made since in the experiment the magnetic field direction is not aligned with the symmetry axis of the dots. Also, while the effective g-factor has been measured for very different values of L , only a small range of radii has been covered in Ref. [4].

D. Phonon-induced spin relaxation rate

An important quantity characterizing the usefulness of quantum dots for spintronics applications is the spin lifetime, which is generally limited by interactions with acoustic phonons. We consider here the most relevant situation for possible applications, namely, an electron initially in the higher sublevel $|i\rangle$ of the lowest Zeeman doublet which relaxes to the lower sublevel $|f\rangle$ due to the emission of a phonon. The rate Γ of this process can be calculated using Fermi's Golden Rule

$$\Gamma = \frac{2\pi}{\hbar} \sum_{\mathbf{Q}, \lambda} |\langle f | U_\lambda(\mathbf{Q}) | i \rangle|^2 [n(Q) + 1] \delta(\Delta E - \hbar\omega_\lambda), \quad (37)$$

where \mathbf{Q} is the phonon momentum. The label $\lambda = \{l, t\}$ refers to the longitudinal and the transverse modes, respectively, and $n(Q)$ is the Bose-Einstein phonon distribution with energy $\hbar\omega_\lambda = \hbar c_\lambda Q$ where c_λ is the sound velocity of the corresponding mode. The energy difference between the two electronic states $\Delta E = E_i - E_f$ determines via the δ -function the energy of the phonons involved in the relaxation process. The potential $U_\lambda(\mathbf{Q})$ comprises both the deformation and the piezoelectric contributions²⁷⁻³⁰ for wurtzite lattice structures. For the longitudinal mode, we have

$$U_l(\mathbf{Q}) = [\Xi_l(\mathbf{Q}) + i\Delta_l(\mathbf{Q})] e^{i\mathbf{Q}\cdot\mathbf{r}} \quad (38)$$

with $\Xi_l(\mathbf{Q})$ being the deformation potential given by

$$\Xi_l(\mathbf{Q}) = \Xi_0 A_l \sqrt{Q}, \quad (39)$$

where Ξ_0 is a bulk-phonon constant. The quantity $A_\lambda = \sqrt{\frac{\hbar}{2V\rho c_\lambda}}$ contains the mass density ρ and the sample volume V . The deformation potential has the same form as in the case of a zincblende structure. The term $\Delta_l(\mathbf{Q})$ accounts for the piezoelectric contribution and upon introducing spherical coordinates (Q, θ_p, φ_p) for the phonon momentum, it reads

$$\Delta_l(\mathbf{Q}) = A_l \frac{1}{Q^{1/2}} \Delta_0 \cos \theta_p (h_{33} - h_x \sin^2 \theta_p), \quad (40)$$

where $h_x = h_{33} - 2h_{15} - h_{31}$. In general, h_{ij} are bulk phonon constants and $\Delta_0 = 4\pi e/\kappa$, where κ is the dielectric constant and e the electronic charge. We emphasize that θ_p is the angle between \mathbf{Q} and the z -axis (defined as the c -axis of the wurtzite structure).

The potential of the transverse phonon mode is given by

$$U_t(\mathbf{Q}) = \Delta_t(\mathbf{Q}) e^{i\mathbf{Q}\cdot\mathbf{r}} \quad (41)$$

with

$$\Delta_t(\mathbf{Q}) = A_t \frac{1}{Q^{1/2}} \Delta_0 \sin \theta_p (h_{15} + h_x \cos^2 \theta_p). \quad (42)$$

We emphasize that in wurtzite lattices the transverse piezoelectric potential has only one term, while in zincblende lattices it has two. The matrix element in Eq. (37) can be factorized, and the rate can be written as

$$\Gamma = \frac{2\pi}{\hbar} \sum_{\mathbf{Q}, \lambda} |M_\lambda(\mathbf{Q})|^2 |\langle f | e^{i\mathbf{Q}\cdot\mathbf{r}} | i \rangle|^2 n(Q) \delta(\Delta E - \hbar\omega_\lambda), \quad (43)$$

where $M_l = \Xi_l(\mathbf{Q}) + i\Delta_l(\mathbf{Q})$ and $M_t = \Delta_t(\mathbf{Q})$. We first note that the modulus of the momentum is fixed by the δ -function. Concerning the integral over the electronic coordinates, we remark that both the initial and the final states denoted by $\Phi_{nm}^{f(i)}(\rho, \phi, z) = \Psi_{nm}^{f(i)}(\rho, \phi) \sqrt{2/L} \sin(n\pi z/L)$ have the same z -dependent factor. Therefore, the integral corresponding to the matrix element in (43) can be further split into two parts by using cylindrical coordinates, leading to

$$|\langle f | e^{i\mathbf{Q}\cdot\mathbf{r}} | i \rangle|^2 = |Z(\theta_p)|^2 |\Upsilon(\theta_p, \varphi_p)|^2. \quad (44)$$

The integral over z can be performed analytically, yielding

$$|Z(\theta_p)|^2 = \frac{2(2\pi n)^4 (1 - \cos q_z)}{q_z^2 [(2\pi n)^2 - q_z^2]^2}, \quad (45)$$

where the definition $q_z = QL \cos(\theta_p)$ has been used. The other integral $\Upsilon(\theta_p, \varphi_p)$ reads

$$\begin{aligned} \Upsilon(\theta_p, \varphi_p) = & \int_0^1 d\rho \rho \left[\left(c_a^f J_{m_f}(K_a^f \rho) + c_b^f J_{m_f}(K_b^f \rho) \right) \left(c_a^i J_{m_i}(K_a^i \rho) + c_b^i J_{m_i}(K_b^i \rho) \right) \right. \\ & + \left. \left(c_a^f d_a^f J_{m_f+1}(K_a^f \rho) + c_b^f d_b^f J_{m_f+1}(K_b^f \rho) \right) \left(c_a^i d_a^i J_{m_i+1}(K_a^i \rho) + c_b^i d_b^i J_{m_i+1}(K_b^i \rho) \right) \right] \\ & \times \int_0^{2\pi} d\varphi \exp [i(m_i - m_f)\varphi] \exp [iQ \sin \theta_p \cos(\varphi_p - \varphi)\rho R] . \end{aligned} \quad (46)$$

The integral over φ can be easily performed by applying the Jacobi-Anger relation

$$\exp [ix \cos \varphi] = \sum_{l=-\infty}^{\infty} i^l J_l(x) \exp [il\varphi] . \quad (47)$$

Upon replacing Eq. (47) in Eq. (46) and carrying out the integration over φ , terms for all values of l vanish except the one with $l = m_f - m_i$. The integral then results in

$$\int_0^{2\pi} d\varphi e^{i(m_i - m_f)\varphi} e^{iQ \sin \theta_p \cos(\varphi_p - \varphi)\rho R} = 2\pi e^{i(m_i - m_f)(\varphi_p - \pi/2)} J_{m_f - m_i}(\rho R Q \sin \theta_p) . \quad (48)$$

As it can be seen in Eq. (48), the complex exponential becomes a common factor in Eq. (46), and leads to $|\Upsilon(\theta_p, \varphi_p)|^2 = f(\theta_p)$, which is not surprising, since the cylindrical symmetry is not broken by the phonon potential.

In addition to the determination of the values of K_a , K_b , and ΔE from numerically solving the quantization condition (24), (26), and (30) as in Sec. IV A, the calculation of the spin relaxation rate still involves an integral over ρ , and a subsequent integration over θ_p (since neither $|\Upsilon(\theta_p, \varphi_p)|^2$ nor $|M_\lambda(\mathbf{Q})|^2$ depend on φ_p , cf. Eqs. (39), (40) and (42)), that we perform numerically as well.

In the numerical evaluation of the relaxation rate, the parameters we use are $\rho = 5900 \text{ kg/m}^3$, $c_l = 4410 \text{ m/s}$, $c_t = 2130 \text{ m/s}$, $\kappa = 15.15$, and $\Xi_0 = 5.8 \text{ eV}$, all taken from Ref. [27]. As the piezoelectric bulk constants for InAs nanowires having wurtzite structure have not been obtained so far from microscopic calculations, we follow the standard prescription^{27,28,31,32} of estimating them from the cubic structure by the use of the relations $h_{15} = h_{31} = (-1/\sqrt{3})h_{14}$ and $h_{33} = (2/\sqrt{3})h_{14}$. For h_{14} we use the value of the zincblende structure case ($3.5 \cdot 10^8 \text{ Vm}^{-1}$ [27]), assuming that at least the order of magnitude of that value should be correct for the wurtzite case. It can be seen from Eqs. (40), (42), and (43) that the relaxation rate due to the piezoelectric contributions is proportional to h_{14}^2 and thus not extremely sensitive to its precise value.

We present in Fig. 5 the results for the spin relaxation rate in a cylindrical dot of length $L = 100 \text{ \AA}$ and radius $R = 275 \text{ \AA}$, as a function of magnetic field, assuming that the initial and final eigenstates in the relaxation process are the two lowest energy states (i.e the first Zeeman-split sublevels). The black curves show the zero-temperature contributions of the different phonon potentials separately. It can be seen that the transverse piezoelectric mode yields the dominant relaxation rate

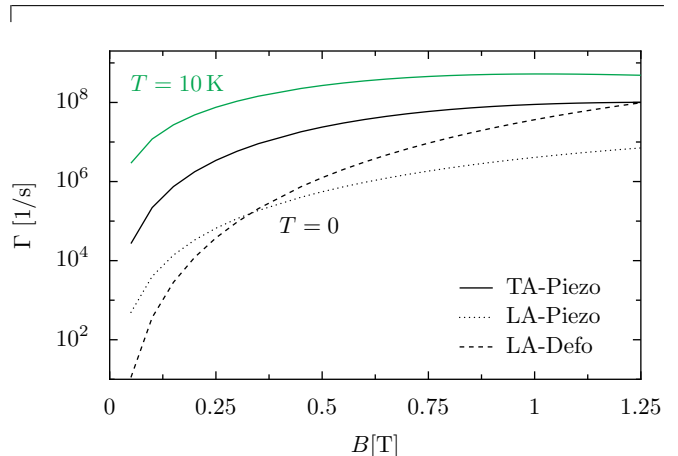


FIG. 5. The calculated contributions of different acoustic-phonon potentials to the spin relaxation rate as a function of magnetic field for cylindrical InAs quantum dots of length $L = 100 \text{ \AA}$ and radius $R = 275 \text{ \AA}$, with wurtzite lattice structure. The black curves correspond to the zero-temperature relaxation rate yielded by the piezoelectric transverse (TA-Piezo; solid), the piezoelectric longitudinal (LA-Piezo; dotted), and the deformation (LA-Defo; dashed) potentials. The green line shows the spin relaxation rate due to TA-Piezo at finite temperature $T = 10 \text{ K}$.

for magnetic field strengths below 1.25 T. Moreover, the relaxation rate strongly increases with the magnetic field strength. This is due to the Zeeman splitting that makes phonons of higher energies relevant where the density of phonon states is increased. Quite long spin lifetimes, of the order of 10 ns, occur for magnetic field strengths around 1 T, and much longer lifetimes are obtained at weaker magnetic fields.

The temperature dependence enters solely through the Bose-Einstein distribution in Eq. (37), such that the increase of the spin relaxation rate with increasing temperature can be easily obtained. The result for the dom-

inating TA-piezo mechanism at 10 K is shown in Fig. 5 (green solid line).

Though it is clearly dominated by the piezoelectric contribution, the order of magnitude of the deformation-coupling caused spin relaxation rates we find is consistent with the one of Ref. [27], where the singlet-triplet relaxation for an InAs nanowire-based quantum dot was calculated. However, in that work, only the deformation coupling was taken into account and assumed to dominate. The same assumption was made in Ref. [28], where the electron spin relaxation in a similar quantum dot was calculated. In both references, the supposed dominance of the deformation over the piezoelectric potential was justified by the fact that they considered small semiconductor nanostructures. As explained in Ref. [33], there is a competition between the two components that depends on the size of the nanostructure. For instance, the leading role of the piezoelectric coupling for weak magnetic fields has been reported³⁴ for quasi-one-dimensional “cigar-like” quantum dots in GaAs nanowires with zincblende structure. For GaAs quantum dots, a crossing between the deformation and piezoelectric-induced rate as a function of the magnetic field was found in Ref. [35]. In our case this occurs as well, though for lower values of magnetic field than those observed in Ref. [35]. For InSb nanowires, numerical calculations show that the deformation potential dominates.^{34,35} That domination has been assumed to be present in general, for all narrow-gap semiconductors.³⁶ In contrast, in recent measurements on an InAs nanowire-based quantum dot,³² the piezoelectric coupling was crucial for the determination of the phonon spectrum.

We find that for InAs, which has a larger band gap than InSb, but smaller than GaAs, the spin relaxation rate is mainly driven by the (transverse) piezoelectric phonon potential for magnetic fields below 1.25 T. Beyond this value, the deformation seems to overcome the piezoelectric contribution, but our theory does not allow us to treat stronger magnetic fields.

V. CONCLUDING REMARKS

Motivated by recent experiments on spin-orbit qubits in InAs nanowire-based quantum dots,⁷ we have calculated the electronic structure of quantum wells and cylindrical quantum dots with wurtzite lattice structure, taking into account the linear and cubic Dresselhaus spin-orbit couplings and a weak applied magnetic field. We found analytical solutions for the energy levels of both types of structures. For quantum dots, we worked along the lines of the solutions previously found in the presence of the linear Rashba spin-orbit coupling.^{17,18} Our obtained solution allowed us to explore the spin texture and the effective g-factor of the energy eigenstates, and, furthermore, we calculated the phonon-induced spin relaxation rate in the ground-state Zeeman doublet.

The energy dispersion of quantum wells shows a strong

influence of the cubic Dresselhaus term. In quasi-two-dimensional structures, the cubic term leads to a thickness-dependent renormalization of the linear term which is of the same order of magnitude as the bare term. This renormalization produces a level crossing of all the subbands (within the range of validity of perturbation theory) that is being reported here for the first time. Another level crossing, which is a consequence of the competition between the linear and the cubic terms, and which has been reported earlier in wurtzite-structure materials, is also obtained here. Although our analytical results are valid for all wurtzite-lattice materials, for concreteness we presented full numerical results for InAs quantum wells only.

The quantum-dot eigenstates have been obtained as linear superpositions of degenerate quantum-well states, and their associated energies calculated as functions of the Dresselhaus coupling constants with and without a relatively weak Zeeman term. Again, a strong influence of the cubic term is observed in the energy levels. The spin texture of the energy eigenstates is shown to be qualitatively modified by the presence of the Dresselhaus spin-orbit coupling. Further studies and applications of these states as qubits should take into account this seldom discussed feature of the states. Our analysis of the effective ground-state g-factor shows a remarkable scaling collapse when the data are plotted as a function of the effective linear in-plane spin-orbit coupling α' , that contains a size-dependent renormalization from the cubic Dresselhaus coupling γ . The obtained results are consistent with existing experimental data⁴ even though the magnetic field orientation is not the same. The scaling of the data indicates that other size-dependent mechanisms are of minor importance. However, the cubic in-plane coupling γ' is expected to become more relevant in the case of very small radius R and/or for the g-factor of higher excited states.

Finally, we have calculated the acoustic-phonon-induced spin relaxation rate between the lowest Zeeman sublevels as a function of magnetic field. The different rates arising from the longitudinal deformation, longitudinal piezoelectric, and transverse piezoelectric contributions for wurtzite structures have been calculated and compared. While our results for the spin relaxation rate due to the deformation mechanism are consistent with those of Ref. [27], we find that, in contrast to what is usually expected for small nanostructures,²⁷ the transverse piezoelectric phonon potential gives the dominant relaxation rate, at least for our case of cylindrical dots.

ACKNOWLEDGMENTS

Acknowledgements: We thank Klaus Ensslin, Renaud Leturcq, and Stevan Nadj-Perge for useful comments and Craig Pryor for helpful correspondence. We gratefully acknowledge support from the ANR through grant ANR-08-BLAN-0030-02, the Collège Doctoral Européen of

Strasbourg, UBACYT 2011-2014, program ECOS Sud-

Mincyt (Action A10E06), and the ITN European Project NanoCTM (Grant agreement 234970).

-
- ¹ Y. Wu, R. Fan, and P. Yang, *Nano Lett.* **2**, 83 (2002).
- ² M. T. Björk, B. J. Ohlsson, T. Sass, A. I. Persson, C. Thelander, M. H. Magnusson, K. Deppert, L. R. Wallenberg, L. Samuelson, *Nano Lett.* **2**, 87 (2002).
- ³ L. J. Lauhon, M. S. Gudiksen, J. Wang, and C. M. Lieber, *Nature* **420**, 57 (2002).
- ⁴ M. T. Björk, A. Fuhrer, A. E. Hansen, M. W. Larsson, L. E. Fröberg, and L. Samuelson *Phys. Rev. B* **72**, 201307(R) (2005).
- ⁵ A. Pfund, I. Shorubalko, K. Ensslin, and R. Leturcq, *Phys. Rev. Lett.* **99**, 036801 (2007); *Phys. Rev. B* **79**, 121306(R) (2009).
- ⁶ C. Fasth, A. Fuhrer, L. Samuelson, V. N. Golovach, and D. Loss, *Phys. Rev. Lett.* **98**, 266801 (2007).
- ⁷ S. Nadj-Perge, S. M. Frolov, E. P. A. M. Bakkers, and L. P. Kouwenhoven, *Nature* **468**, 1084 (2010).
- ⁸ S. Nadj-Perge, V. S. Pribiag, J. W. G. van den Berg, K. Zuo, S. R. Plissard, E. P. A. M. Bakkers, S. M. Frolov, and L. P. Kouwenhoven, *Phys. Rev. Lett.* **108**, 166801 (2012).
- ⁹ V. Mourik, K. Zuo, S. M. Frolov, S. R. Plissard, E. P. A. M. Bakkers, and L. P. Kouwenhoven, *Science* **336**, 1003 (2012).
- ¹⁰ E. I. Rashba and A. L. Efros, *Appl. Phys. Lett.* **83**, 5295 (2003).
- ¹¹ V. N. Golovach, M. Borhani, and D. Loss, *Phys. Rev. B* **74**, 165319 (2006).
- ¹² M. Koguchi, H. Kakibayashi, M. Yazawa, K. Hiruma, and T. Katsuyama, *Jpn. J. Appl. Phys.* **31**, 2061 (1992).
- ¹³ L. C. Lew Yan Voon, M. Willatzen, M. Cardona, and N. E. Christensen, *Phys. Rev. B* **53**, 10703 (1996).
- ¹⁴ W. T. Wang, C. L. Wu, S. F. Tsay, M. H. Gau, I. Lo, H. F. Kao, D. J. Jang, J. C. Chiang, M. E. Lee, Y. C. Chang, C. N. Chen, and H. C. Hsueh, *Appl. Phys. Lett.* **91**, 082110 (2007).
- ¹⁵ J. Y. Fu and M. W. Wu, *J. Appl. Phys.* **104**, 093712 (2008).
- ¹⁶ A. De and Craig E. Pryor, *Phys. Rev. B* **81**, 155210 (2010).
- ¹⁷ E. N. Bulgakov and A. F. Sadreev, *JETP Lett.* **73**, 505 (2001).
- ¹⁸ E. Tsitsishvili, G. S. Lozano, and A. O. Gogolin, *Phys. Rev. B* **70**, 115316 (2004).
- ¹⁹ N. J. Harmon, W. O. Putikka, and R. Joynt, *Appl. Phys. Lett.* **98**, 073108 (2011).
- ²⁰ G. A. Intronati, P. I. Tamborenea, D. Weinmann, and R. A. Jalabert, *Phys. Rev. Lett.* **108**, 016601 (2012).
- ²¹ P. Nozières and C. Lewiner, *J. Phys. (Paris)* **34**, 901 (1973).
- ²² H.-A. Engel, E. I. Rashba, and B. I. Halperin, in *Handbook of Magnetism and Advanced Magnetic Materials*, Vol. 5, H. Kronmüller and S. Parkin (eds.) (John Wiley & Sons Ltd, Chichester, 2007).
- ²³ E. I. Rashba, *Sov. Phys. Solid State* **2**, 1109 (1960). Y. A. Bychkov and E. I. Rashba, *JETP Lett.* **39**, 78 (1984); *J. Phys. C* **17**, 6039 (1984).
- ²⁴ M. Abramowitz and I. A. Stegun (eds.), *Pocketbook of mathematical functions*, relations 9.1.27 (Harri Deutsch, Frankfurt 1984).
- ²⁵ Wan-Tsang Wang, C. L. Wu, J. C. Chiang, Ikai Lo, H. F. Kao, Y. C. Hsu, W. Y. Pang, D. J. Jang, Meng-En Lee, Yia-Chung Chang, and Chun-Nan Chen, *J. Appl. Phys.* **108**, 083718 (2010).
- ²⁶ A. De and Craig E. Pryor, *Phys. Rev. B* **76**, 155321 (2007).
- ²⁷ Y. Yin, *Semicond. Sci. Technol.* **25**, 125004 (2010).
- ²⁸ Y. Yin and M. W. Wu, *J. Appl. Phys.* **108**, 063711 (2010).
- ²⁹ J. D. Zook, *Phys. Rev.* **136**, 869 (1964).
- ³⁰ G. Kokolakis, F. Compagnone, A. Di Carlo, and P. Lugli, *Phys. Stat. Sol.(a)* **195**, 618 (2003).
- ³¹ A. Bykhovski, B. Gelmont, M. Shur, and A. Khan, *J. Appl. Phys.* **77**, 1616 (1995).
- ³² C. Weber, A. Fuhrer, C. Fasth, G. Lindwall, L. Samuelson, and A. Wacker, *Phys. Rev. Lett.* **104**, 036801 (2010).
- ³³ T. Takagahara, *Phys. Rev. Lett.* **71**, 3577 (1993).
- ³⁴ C. L. Romano, P. I. Tamborenea, and S. E. Ulloa, *Phys. Rev. B* **74**, 155433 (2006).
- ³⁵ C. F. Destefani and S. E. Ulloa, *Phys. Rev. B* **72**, 115326 (2005).
- ³⁶ C. L. Romano, G. E. Marques, L. Sanz, and A. M. Alcalde, *Phys. Rev. B* **77**, 033301 (2008).